Curvature-induced electron localization in developable Möbius-like nanostructures

A P Korte and G H M van der Heijden

Centre for Nonlinear Dynamics, University College London, Chadwick Building,
Gower Street, London WC1E 6BT, UK

E-mail: a.korte@ucl.ac.uk and g.heijden@ucl.ac.uk

Abstract

We study curvature effects and localization of non-interacting electrons confined to developable one-sided elastic sheets motivated by recent nanostructured origami techniques for creating and folding extremely thin membrane structures. The most famous one-sided sheet is the Möbius strip but the theory we develop allows for arbitrary linking number. Unlike previous work in the literature we do not assume a shape for the elastic structures. Rather, we find the shape by minimizing the elastic energy, i.e., solving the Euler–Lagrange equations for the bending energy functional. This shape varies with the aspect ratio of the sheet and affects the potential experienced by the particles. Depending on the link there is a number of singular points on the edge of the structure where the bending energy density goes to infinity, leading to deep potential wells. The inverse participation ratio is used to show that electrons are increasingly localized to the higher-curvature regions of the higher-width structures, where sharp creases radiating out from the singular points could form channels for particle transport. Our geometric formulation could be used to study transport properties of Möbius strips and other components in nanoscale devices.

(Some figures in this article are in colour only in the electronic version)

1. Introduction

Progress in techniques for the manipulation of very small structures (usually referred to as nanostructures) is constantly opening new perspectives for the fabrication of electromechanical devices such as force probes, capacitors, resonators, etc with potentially unusual physical properties. There is, therefore, significant interest in the relationship between geometry (and topology) and transport and optical properties such as electrical conductance and photoluminescence. Theoretical work has looked at curvature-induced effective quantum potentials experienced by particles confined to a surface. Explicit potentials have been obtained for a few idealized shapes such as a helical nanotube [1], helicoidal ribbons [2] and elliptical tori [3]. Gravesen and Willatzen study eigenstates of a particle confined to an inextensible Möbius strip using a three-parameter approximation of its equilibrium shape [4]. States and localization of particles confined to an ellipsoidal quantum dot are studied in [5]. Localized states in helicoidal strips are considered in [6]. We note that the trapping of modes in curved structures also occurs in macroscopic systems such as elastic plates [7] and rods [8].

Recent technological developments, such as nanostructured origami [9] and strain engineering of nanomembranes [10], have demonstrated the possibility of producing extremely thin membrane structures that can be folded in a controlled fashion. The nanomembranes created this way do not only include semiconductors. Indeed, silicon nanomembranes (SiNMs), consisting of the same material as bulk Si-based semiconductors, have been shown to become electrical conductors when the membrane is sufficiently thin. Parallel developments have made it possible to confine electrons to lower spatial dimensions, as in quantum dots, wires, ribbons and wells. In [11] the authors report on polycrystalline and single-crystal silicon thin-film transistor (TFT) technology applied to Si nanowire thin films and CdS nanoribbons. Scanning tunnelling spectroscopy experiments of so-called surface state electrons, which move freely parallel to the surface of noble metals but are confined to a narrow surface layer in the perpendicular direction, are discussed in [12].

Crystal structures with varying linking number (including Möbius strips) have also been fabricated recently [13], opening the possibility of studying the topological effect of link on transport properties. We furthermore note that wavefunctions

have been calculated for graphene nanoribbons of varying linking number (and fixed aspect ratio) [14].

Here we consider curvature effects and localization in one-sided surfaces. Such surfaces have half-integer linking number Lk. The best known example of such a surface is the Möbius strip, with $Lk = 1/2$, but the theory we develop also allows for larger values of Lk. Since a sufficiently thin elastic surface deforms by bending only (i.e., no stretching) [15, 16], we will consider isometric deformations of an intrinsically flat rectangular sheet.

Unlike previous work in the literature we do not assume a shape for the elastic structures. Rather, we find the shape by minimizing the elastic energy, i.e., solving the Euler–Lagrange equations for the bending energy functional. This allows us to account for the change of shape of the structure under varying aspect ratio of the sheet and the effect this has on the electron states. Interestingly, the minimum-energy solution reveals the existence of singular points on the edge of the structure where the bending energy density tends to infinity, giving rise to deep surface potential wells.

We should note that the theory also applies to (double-sided) surfaces with integer link, such as the cylinder ($Lk = 0$) or the figure-of-eight sheet ($Lk = 1$). However, these surfaces are uniform in their axial direction and their shape does not depend on the aspect ratio in an essential way. As a result of this, the quantum mechanical problem decouples into lower-dimensional problems that are easier to solve [17]. These surfaces have no singular points and will not further be considered here.

We use the inverse participation ratio to show that electrons are increasingly localized to the higher-curvature regions of the higher-width structures, where sharp creases radiating out from the singular points appear to form channels for particle transport. Our geometric formulation could be used to study transport properties of Möbius strips and other folded-sheet components in nanoscale devices.

2. The quantum mechanics of a particle bound to a surface

We consider a particle confined to an intrinsically flat thin sheet folded into a closed structure. We assume that self-interaction of the sheet (e.g., of the van der Waals type if surface patches come within close proximity) and entropic effects can be neglected, as a first-order approximation, compared to the local deformation energy. Thus the shape of the surface is purely determined by the elastic energy. If required, corrections to the shape due to entropic and interaction effects can be computed [18], but we shall not need this here. We furthermore assume that the sheet behaves as an isotropic elastic continuum (i.e., is elastically equivalent in all directions). This will be the case for isotropic single crystals or isotropic bodies, and will be a good approximation for polycrystalline materials whose component crystals are sufficiently small compared to the radii of curvature of the deformed sheet. Such an isotropic material can be characterized by two elastic constants, the modulus of compression and the shear modulus, or, equivalently, Young's modulus and Poisson's ratio.

All the above assumptions are reasonable for structures at the mesoscopic scale (tens to thousands of angstroms) or larger. This coarse-grained modelling of apparently disparate materials emphasizes the universality of common properties derived from the geometry and topology of a flexible sheet deforming in three-dimensional space, rather than from its chemical details.

To formulate the quantum mechanics of a particle moving on the surface of a mesoscopic structure as described in the Introduction we assume a strong one-dimensional confining scalar potential V normal to the surface [19, 20]. The particle's Cartesian coordinates in a small neighbourhood of the surface are expressed as

$$\mathbf{R}(q_1, q_2, q_3) = \mathbf{x}(q_1, q_2) + q_3 \mathbf{N}(q_1, q_2), \qquad (1)$$

where $\mathbf{x}$ is an embedding of the surface in $\mathbb{R}^3$ and q_1, q_2 define a local coordinate system on the surface; q_3 is the distance from the surface in the direction of the unit normal to the surface $\mathbf{N}$.

The Laplacian in the curvilinear coordinates q_A defined by this parametrization is $\partial_A G^{AB} |G|^{1/2} \partial_B$, $A, B = 1, 2, 3$ where $G_{AB} = \partial_A \mathbf{R} \cdot \partial_B \mathbf{R}$ is the metric, and $|G|$ its determinant. The normalization of the wavefunction ϕ is given by $\int |\phi|^2 |G|^{1/2} \, \mathrm{d}^3 q = 1$. The wavefunction is then scaled according to $\Psi = (|G|^{1/4}/|g|^{1/4})\phi$, where $|g|$ is the determinant of $g_{ij} = \partial_i \mathbf{x} \cdot \partial_j \mathbf{x}$, $i, j = 1, 2$, the metric of the surface. The Hamiltonian therefore transforms as $H \rightarrow (|G|^{1/4}/|g|^{1/4})H(|g|^{1/4}/|G|^{1/4})$ so that $H\Psi = E\Psi$. The normalization of Ψ is then given by $\int \mathrm{d}q_1 \, \mathrm{d}q_2 \, |g|^{1/2} \, \mathrm{d}q_3 \, |\Psi|^2 = 1$. We do not make the further scaling $\Psi' = |g|^{1/4}\Psi$ so that the wavefunction Ψ' would then be normalized with Euclidean norm [1]. The determinant $|G|$ can easily be directly calculated from G_{AB} as $|G| = |g|f^2$, with $f = 1 - 2Mq_3 + Kq_3^2$, where K is the Gaussian curvature and M the mean curvature of the surface $\mathbf{x}$ [17, 19]. Implementing the constraint imposed by a confining potential of the form $V(q_3) = \omega^2 q_3^2/2 + \mathrm{O}(q_3^3)$, and rescaling according to $\omega \rightarrow \omega/\epsilon$, $q_3 \rightarrow \epsilon^{1/2} q_3$, with ϵ a small dimensionless parameter, gives the expansion $\epsilon H = H_0 + \epsilon H_1 + \mathrm{O}(\epsilon^{3/2})$, with $H_0 = -\hbar^2/2m \, \partial^2/\partial q_3^2 + \omega^2 q_3^2/2$ and the Hamiltonian H_1 on the surface equal to (see [20])

$$-\frac{\hbar^2}{2m} \left(\frac{1}{|g|^{1/2}} \partial_i g^{ij} |g|^{1/2} \partial_j \right) + \frac{\hbar^2}{8m} g^{ij} g^{kl} \left(h_{ij} h_{kl} - 2h_{ik} h_{jl} \right), \qquad (2)$$

where h_{ij} are the coefficients of the second fundamental form, i.e., $h_{ij} = \partial_i \mathbf{x} \cdot \partial_j \mathbf{N}$, $i, j = 1, 2$. This is equation (21) in the general treatment of m-dimensional embeddings in n-dimensional Euclidean space of [20] specialised to our case of a two-dimensional surface in three-dimensional space (in this case the coefficients of the normal fundamental form vanish, i.e., $\mathbf{N} \cdot \partial_i \mathbf{N} = 0$). It is straightforward to show that $g^{ij} g^{kl}(h_{ij} h_{kl} - 2h_{ik} h_{jl})/8 = -(M^2 - K)/2$. The wavefunction Ψ then separates in the form

$$\Psi(q_1, q_2, q_3) = \chi(q_1, q_2)\psi(q_3), \qquad (3)$$

giving for the surface wavefunction the two-dimensional Schrödinger equation

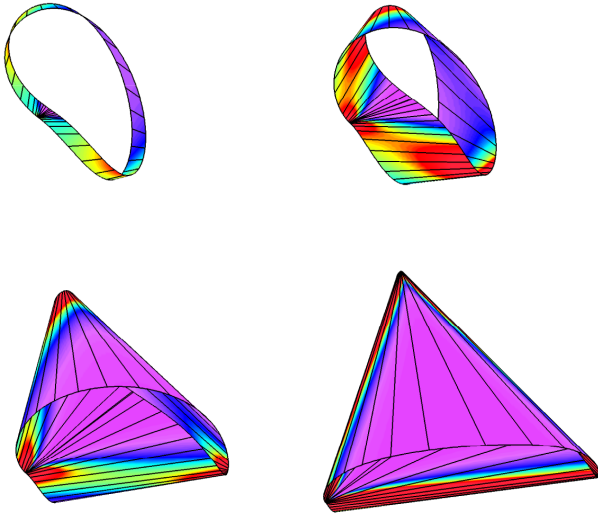$$-\frac{\hbar^2}{2m}(\Delta + M^2 - K)\chi = E\chi, \qquad (4)$$

Figure 1. $Lk = 1/2$ structures of aspect ratio $L/2w = 30, 2\pi, \pi,$ $2\pi/3$ (top left to bottom right) with generators shown. The colouring changes according to the local bending energy density, from violet for regions of low bending to red for regions of high bending (scales are individually adjusted). Note the singularity on the edge of the strip.

where Δ is the Laplace–Beltrami operator of the surface and E is zero order in the thickness of the surface [20].

A sufficiently thin elastic surface will deform by bending only [15] and therefore deform isometrically. If such a surface is flat in its unstressed state it will remain so under deformation and therefore have zero Gaussian curvature, $K = 0$ [21]. It is said to be developable. The bending energy of a surface of thickness $2h$ can then be written as the following integral over the surface of the strip [22]:

$$U = 2D \int \int M^2 \, \mathrm{d}^2\mathbf{x},\qquad(5)$$

where $D = 2E_\mathrm{Y}h^3/[3(1 - \nu^2)]$ is the flexural rigidity, ν is Poisson's ratio and E_Y is Young's modulus.

If $\mathbf{r}(s)$ is a parametrization of the centreline of the strip, s being arclength, then

$$\mathbf{x}(s, t) = \mathbf{r}(s) + t[\mathbf{b}(s) + \eta(s)\mathbf{t}(s)]$$
$$\tau(s) = \eta(s)\kappa(s),\qquad s \in [0, L], \quad t \in [-w, w]\qquad(6)$$

is a parametrization of an embedded developable strip of length L and width $2w$ [23]. Here $\mathbf{t}$ and $\mathbf{b}$ are two unit vectors of the Frenet frame $\{\mathbf{t}, \mathbf{n}, \mathbf{b}\}$ of tangent, principal normal and binormal to the centreline, while κ and τ are, respectively, the curvature and torsion of the centreline, which uniquely specify (up to Euclidean motions) the centreline of the strip [21]. The surface, in turn, is completely determined by the centreline of the structure. The straight lines $s = $ const. are the generators of the surface. For this surface parametrization, the mean curvature can be easily calculated using the coefficients of the first and second fundamental forms of the surface as

$$M = -\frac{\kappa}{2}\frac{1 + \eta^2}{1 + t\eta'}.\qquad(7)$$

When M is substituted into (5), with the element of area given by $\mathrm{d}^2\mathbf{x} = \|\mathbf{x}_s \times \mathbf{x}_t\| \, \mathrm{d}s \, \mathrm{d}t = (1 + t\eta') \, \mathrm{d}s \, \mathrm{d}t$, the t integration can be carried out [24] giving

$$U = Dw \int_0^L g(\kappa, \eta, \eta') \, \mathrm{d}s,\qquad(8)$$

with

$$g(\kappa, \eta, \eta') = \kappa^2(1 + \eta^2)^2 \frac{1}{2w\eta'} \log\left(\frac{1 + w\eta'}{1 - w\eta'}\right)\qquad(9)$$

and $\eta' \equiv \mathrm{d}\eta/\mathrm{d}s$. Minimization of this elastic energy functional is a one-dimensional variational problem cast in a form that is invariant under Euclidean motions. Following [16, 25], the Euler–Lagrange equations can be immediately written down in the form of six balance equations for the components of the internal force $\boldsymbol{F}$ and moment $\boldsymbol{M}$ in the directions of the Frenet frame of tangent, principal normal and binormal, $\boldsymbol{F} = (F_t, F_n, F_b)^\mathrm{T}$, $\boldsymbol{M} = (M_t, M_n, M_b)^\mathrm{T}$, and two scalar equations:

$$\boldsymbol{F}' + \boldsymbol{\omega} \times \boldsymbol{F} = \boldsymbol{0}, \qquad \boldsymbol{M}' + \boldsymbol{\omega} \times \boldsymbol{M} + \boldsymbol{t} \times \boldsymbol{F} = \boldsymbol{0}, \quad (10)$$

$$\partial_\kappa g + \eta M_t + M_b = 0, \qquad (\partial_{\eta'} g)' - \partial_\eta g - \kappa M_t = 0, \quad (11)$$

where $\boldsymbol{\omega} = \kappa(\eta, 0, 1)^\mathrm{T}$ is the curvature vector. The shape of the strip's centreline is found by numerically solving these equations in conjunction with the usual Frenet–Serret equations

$$\mathbf{t}' = \kappa\mathbf{n}, \qquad \mathbf{n}' = -\kappa\mathbf{t} + \tau\mathbf{b}, \qquad \mathbf{b}' = -\tau\mathbf{n}, \quad (12)$$

and the centreline equation $\mathbf{r}' = \mathbf{t}$, subject to boundary conditions that prescribe the appropriate link [16]. The surface of the strip is then obtained from (6). For example, $Lk = 1/2$ structures of increasing aspect ratio are shown in figure 1.

Introducing rectangular coordinates (u^1, u^2) by developing the surface into a rectangle,

$$u^1 = s + t\eta(s), \qquad u^2 = t,\qquad(13)$$

Δ in (4) is then the usual planar Laplacian and M^2 provides a geometry-induced quantum potential well (see figures 4 and 9). We therefore solve

$$-\frac{\hbar^2}{2m}(\partial_1^2 + \partial_2^2 + M^2)\chi = E\chi,\qquad(14)$$

subject to the boundary conditions

$$\chi(u^1, u^2 = -w) = \chi(u^1, u^2 = w) = 0,\qquad(15)$$

$$\chi(u^1 + 2L, u^2) = \chi(u^1, u^2),\qquad(16)$$

where (16) is the requirement of the single-valuedness of the wavefunction [26, 27], known as the periodic (or Born–von Karman) boundary condition [28], and (15) that the particle is confined to the width of the strip.
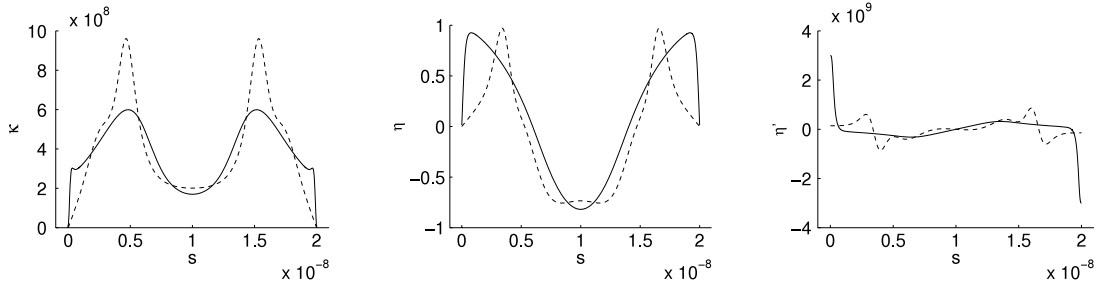
Figure 2. Comparison between the exact shape (solid curves) and the shape obtained from the three-parameter Gravesen–Willatzen approximation (17) (dashed curves) of κ, η, η' as a function of arclength $s \in [0, L]$ for $Lk = 1/2$, $L/2w = 30$, $L = 200$ Å.
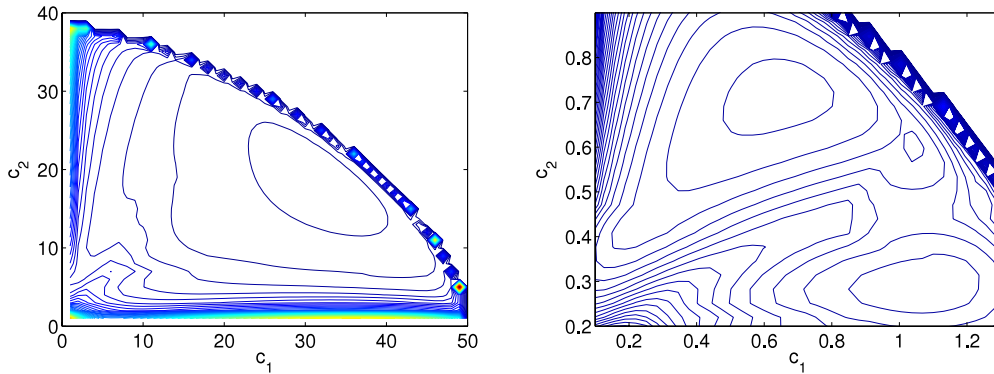

Figure 3. Bending energy versus parameters c_1, c_2 for $L/2w = 30$ (left) and $L/2w = 2\pi$ (right) ($Lk = 1/2$).
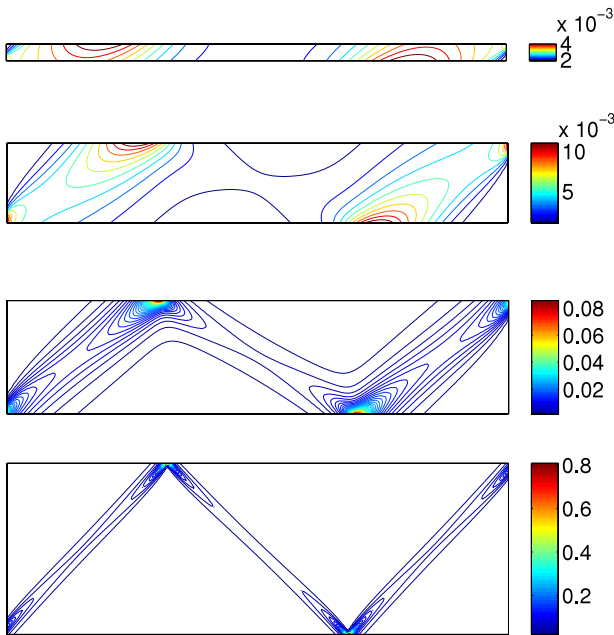

Figure 4. Scaled mean curvature squared of developed strip, $\frac{\hbar^2}{2m}M^2$, in eV, for $Lk = 1/2$ and $L/2w = 30, 2\pi, \pi, 2\pi/3$ (top to bottom). $u_1 \in [0, L], u_2 \in [-w, w], L = 200$ Å.

3. Numerical results and discussion

3.1. Exact Möbius shapes and the Gravesen–Willatzen approximation

Shown in figure 1 are the exact $L/2w = 30, 2\pi, \pi, 2\pi/3$ Möbius structures, with generators shown, of linking number 1/2, as calculated in [16]. The colouring changes according to the local bending energy density, from violet for regions of low bending to red for regions of high bending. The linking number Lk of the (closed) centreline of a strip is equal to the linking number of the (closed) strip minus the number of right-handed turns the strip makes about its centreline (the twist Tw), where the linking number of the strip can be obtained by counting overcrossings [29].

Shown in figure 2 are κ, η, η' as a function of the arclength, s, for the exact shape (solid curves) of the free-standing Möbius strip shown at the top left of figure 1, for $L/2w = 30$, compared with the three-parameter approximation used in [4]. This approximation to the centreline of the strip is given by

$$\mathbf{r}(u) = (c_1 \sin u, c_2 \sin u(1-\cos u), 2c_3(1-\cos u)^3/3), \quad (17)$$

with $u \in [0, 2\pi]$. For this large aspect ratio, corresponding to the dimensions of ribbon-shaped crystals of NbSe$_3$ Möbius shell structures that have recently been fabricated [13] the bending energy corresponding to (17) is easily minimized [4, 16, 24]. The constraint that the length of the strip must equal L allows one of the three parameters, say c_3, to be eliminated, allowing a two-dimensional visualization of the bending energy in the remaining two parameters. For $L/2w = 30$, we obtain a single minimum, as shown in figure 3 (left), as obtained in [4]. For smaller aspect ratios (larger widths), however, as considered in [16], e.g. $L/2w = 2\pi$, there are three candidate minima, as shown in figure 3 (right), none of which satisfy the constraint that ensures that
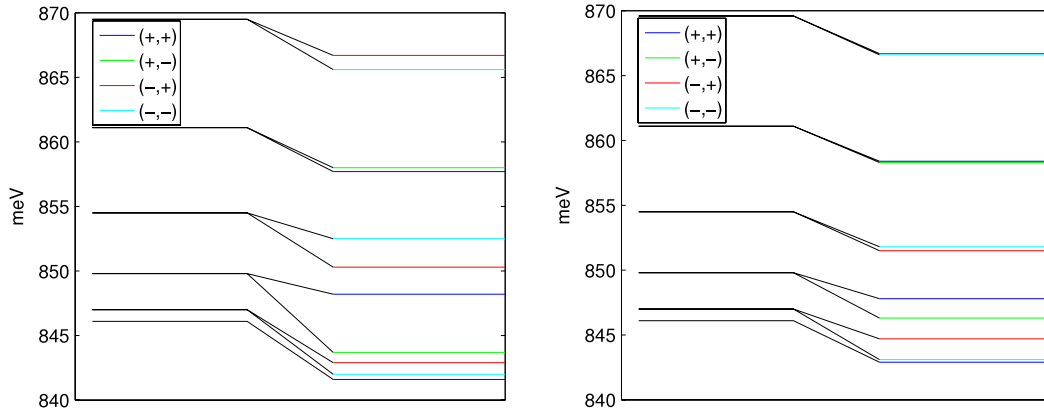
Figure 5. Energy level splittings in meV for $Lk = 1/2$, $L/2w = 30$, $L = 200$ Å, comparing the Gravesen–Willatzen approximation (left) with the exact shape (right).

the generators do not intersect in the interior of the strip [4, 24],

$$|\eta'(u)| \leqslant w^{-1} \qquad (18)$$

(corresponding to avoidance of singularities of M in (7)), indicating the limitations of approximation (17) even for modest strip widths in representing a realistic material strip. In order to calculate the shapes of Möbius structures of higher widths, shown in figures 1 and 8, we therefore solve the equilibrium equations (10) and (11) to obtain κ and η of the exact shape. This allows the energy density M^2 to be obtained via (7), which is required to calculate wavefunctions in (14). It turns out that irrespective of the aspect ratio the equilibrium solution of the strip always satisfies (18). Moreover, there is always exactly one point on the edge of the strip where (18) is satisfied as an equality (see figure 1). This point corresponds to a singular point of infinite bending energy density and leads to a deep quantum potential well.

3.2. Wavefunction symmetry

As illustrated in figure 2, κ and η have even reflection symmetry about $s = L/2$, whereas η' has odd reflection symmetry. This, through (13), induces the following transformation in (u^1, u^2):

$$u^1 \rightarrow L - u^1, \qquad u^2 \rightarrow -u^2. \qquad (19)$$

The Hamiltonian $\mathcal{H} = -\frac{\hbar^2}{2m}(\nabla^2 + M^2)$ is invariant under this transformation since M^2 is. Therefore non-degenerate states are such that

$$\chi(u^1, u^2) = \pm\chi(L - u^1, -u^2). \qquad (20)$$

Similarly, $\mathcal{H}$ is invariant under the transformation

$$u^1 \rightarrow u^1 + L, \qquad u^2 \rightarrow -u^2, \qquad (21)$$

itself induced by the transformation $s \rightarrow s + L$, with corresponding parity eigenstates

$$\chi(u^1, u^2) = \pm\chi(u^1 + L, -u^2). \qquad (22)$$

Equation (22) can be recognized as the Bloch or Floquet theorem for periodic potentials:

$$\chi(u^1 + L, u^2) = e^{ikL}\chi(u^1, -u^2), \qquad (23)$$

which, given the periodic boundary condition (16), gives $kL = n\pi$, with n an integer. Equation (23) then gives (22).

The requirement $u^2 \rightarrow -u^2$ for invariance of M^2 under the $s \rightarrow s + L$ translation comes about because we use a continuously varying $\{\mathbf{t}, \mathbf{n}, \mathbf{b}\}$ frame moving along the centreline, changing to an anti-Frenet frame to avoid a Frenet frame flip where $\kappa = 0$ ($\mathbf{n} \rightarrow -\mathbf{n}$), which therefore defines the coordinate system used in u^1 and u^2. In addition, we therefore require that $\eta \rightarrow -\eta$, $\eta' \rightarrow -\eta'$ and $\kappa \rightarrow -\kappa$, under $s \rightarrow s + L$, to define the $\{\mathbf{t}, \mathbf{n}, \mathbf{b}\}$ frame used. Otherwise, if the Frenet frame is used throughout, it flips under translation, and $u^2 \rightarrow -u^2$ would not be required.

Thus four different symmetry eigenstates are considered: even and odd symmetry under translation by L, and even and odd reflection symmetry in the line $u^1 = L/2$, each with $u^2 \rightarrow -u^2$. We denote, for example, a state as $(-, +)$, if it is odd under translation by L, and even under reflection. Using (20) and (22) one then derives boundary conditions on the wavefunction at u^1 equal to 0 or L. For example, wavefunctions for states of opposite translation and reflection parity vanish on $u^1 = 0$ or L. Using (22), one has $\chi(0, u^2) = \pm\chi(L, -u^2)$.

Reflection symmetry, (20), allows the domain for the numerical computation to be reduced to half the strip. We used a second-order finite-difference (FD) scheme, where M is given by (7) with κ, η, η' as obtained from the numerical solutions from [16], calculating the eigenvalues and eigenstates with MATLAB. For the $(+, +)$ and $(-, -)$ states, using the five-point stencil, one needs an FD equation for each unknown on the $u^1 = 0$ boundary, i.e., one needs to step outside the domain. In order to do this, note that for small $u^1 < 0$, $M^2(u^1, u^2) = M^2(2L - |u^1|, u^2)$ (we are at the same point—this device just makes the first slot in the argument of M^2 positive) $= M^2(L - |u^1|, -u^2)$ (as $\mathbf{b}$ has changed sign and we are exactly under the surface from where we started) $= M^2(L + |u^1|, -u^2)$ (by symmetry and the binormal
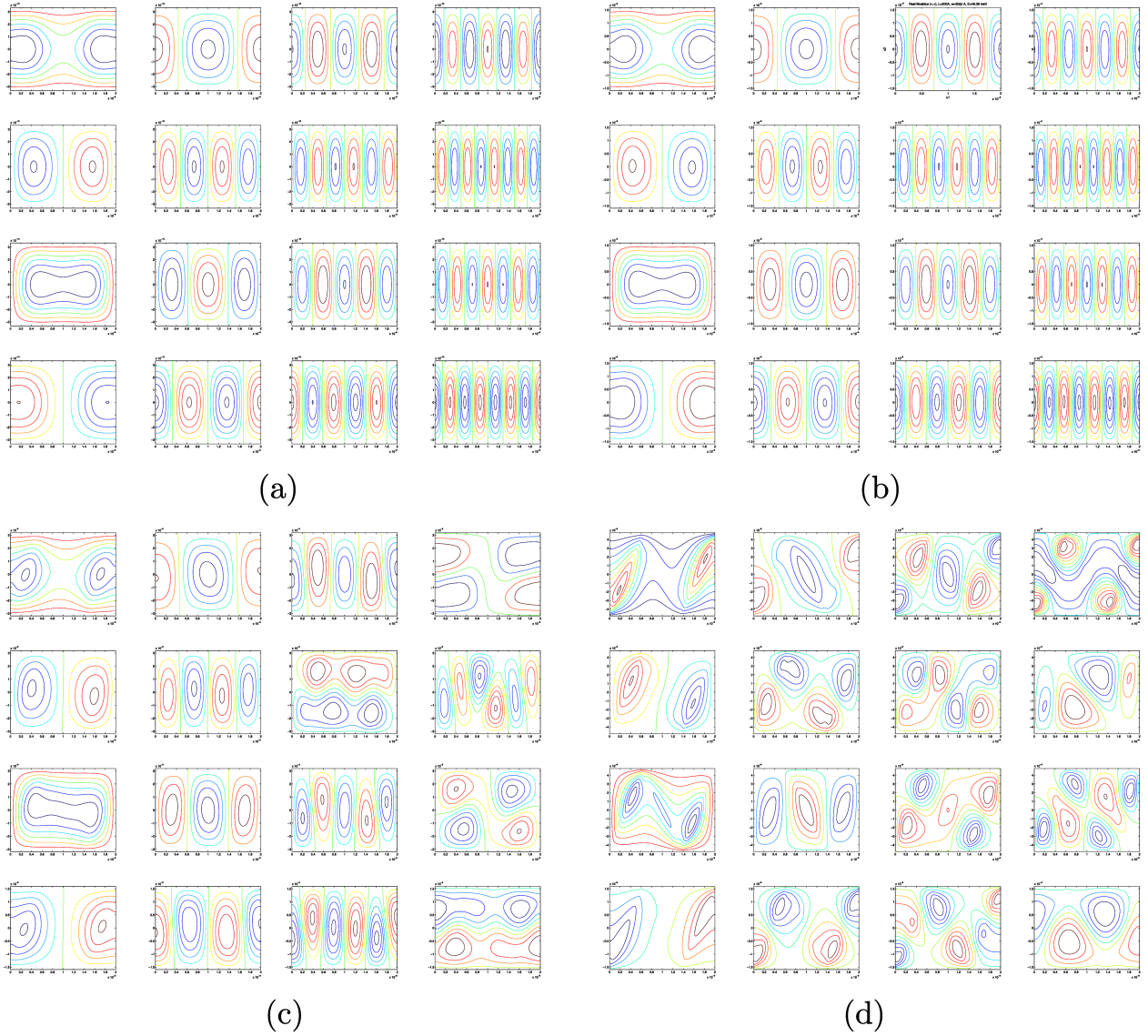
Figure 6. Lowest energy wavefunctions, $Lk = 1/2$. For each plot, the horizontal axis is $u^1 \in [0, L]$, $L = 200$ Å, the vertical axis is $u^2 \in [-w, w]$. In each subfigure the lowest energy wavefunctions for each parity are shown using the order $(+, +)$, $(+, -)$, $(-, +)$, $(-, -)$ for the first, second, third and fourth rows respectively. The lower right subfigure shows localization to the sharp zigzag-patterned creases of the bottom plot in figure 4. (a) $L/2w = 30$; (b) $L/2w = 2\pi$; (c) $L/2w = \pi$; (d) $L/2w = 2\pi/3$.

has not changed sign under the small translation by $2|u^1|$) $= M^2(|u^1|, u^2)$ (as **b** has changed sign when we return to the same neighbourhood to where we started).

The distinction of states under translation by L enables us to distinguish between particles *on* the strip (period $2L$, cf [30], i.e., a single channel with zero hopping parameter) from those *in* the strip (period L), the former allowing negative parity eigenstates under translation by L. A prime motivating factor for the parity formulation was that without imposing (20), we found the FD scheme skips some $(+, +)$ eigenstates [31] when solving over $[0, L]$. The results were verified using finite elements with periodic boundary conditions under translation, which did not require a specification of reflection symmetry to avoid the skipping problem.

It is worth considering the symmetry of the flat-Möbius states, obtained by solving (14) with M^2 set to zero. We

modify the treatment of [4], which considers only the $(+, +)$ and $(+, -)$ states, to allow for all parity eigenstates of period $2L$. There are four independent combinations of eigenstates:

$$\chi_1(u^1, u^2) = \cos(m_1\pi u^1/2L) \cos((2n + 1)\pi u^2/2w),$$
$$\chi_2(u^1, u^2) = \sin(m_2\pi u^1/2L) \cos((2n + 1)\pi u^2/2w),$$
$$\chi_3(u^1, u^2) = \cos(m_3\pi u^1/2L) \sin(n\pi u^2/w),$$
$$\chi_4(u^1, u^2) = \sin(m_4\pi u^1/2L) \sin(n\pi u^2/w),$$

(24)

with $n = 0, 1, 2, \ldots$, $m_i = 0, 2, 4, 6, 8, \ldots$ and either $2mE/\hbar^2 = (m_i\pi/2L)^2 + ((2n + 1)\pi/2w)^2$ for χ_1, χ_2 or $2mE/\hbar^2 = (m_i\pi/2L)^2 + (n\pi/w)^2$ for χ_3, χ_4, respectively. It is understood that $m_i = 0$ and $n = 0$ are excluded if inside a sin function. The $(+, +)$ states are then given by $m_1/2$ even, $m_3/2$ odd, the $(+, -)$ states by $m_2/2$ even, $m_4/2$ odd, the
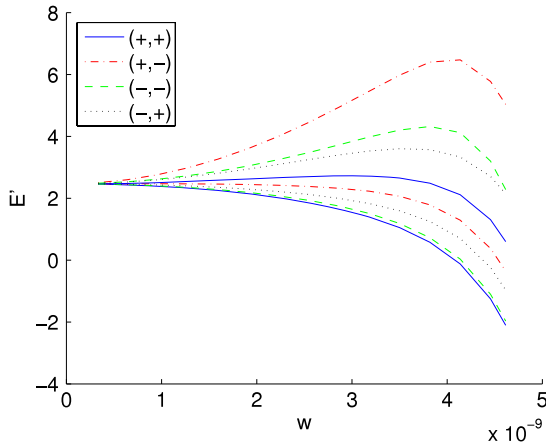
Figure 7. Dimensionless energy, E', for the lowest one- and two-node energy eigenstates for each parity ($Lk = 1/2$).

Figure 8. $Lk = 3/2$ structures of aspect ratio $L/2w = 9.36, 4.72, 4.49, 4.22$ (top left to bottom right) with generators shown. The colouring changes according to the local bending energy density, from violet for regions of low bending to red for regions of high bending (scales are individually adjusted).

$(-, +)$ states by $m_2/2$ odd, $m_4/2$ even, and the $(-, -)$ states by $m_1/2$ odd, $m_3/2$ even. There are two non-degenerate states: the $(+, +)$ state with $m_1 = 0$, $n = 0$ and the $(-, -)$ state with $m_3 = 0$, $n = 1$. Otherwise, the $(+, +)$ states are doubly degenerate with the $(+, -)$ states, the $(-, +)$ states with the $(-, -)$ states. If arbitrary independent linear combinations are taken of the $(+, +)$ states in χ_1 ($m_1/2$ even) and the $(+, -)$ states of χ_2 ($m_2/2$ even) or the $(+, +)$ states in χ_3 ($m_3/2$ odd) and the $(+, -)$ states of χ_4 ($m_4/2$ odd), then one obtains the states of [4], but these are not eigenstates of the reflection parity operator. For the small width in [4], $L/2w = 30$, the non-degenerate ground state has $m_1 = 0$, the doubly degenerate first excited states have $m_1/2 = 2$, $m_2/2 = 2$ and the doubly degenerate second excited states have $m_1/2 = 4$, $m_2/2 = 4$. The ground state has no nodes, the first excited states have two nodes and the second excited states four nodes.

3.3. Single-twist Möbius strip: $Lk = 1/2$

Shown in figure 4 are contour plots of M^2 for the structures shown in figure 1 of increasing widths, which form the potential wells which scatter the standing waves of electrons confined to the strip. For clarity, the outer boundary is omitted, as there are singularities in M^2 there for $|\eta'(s)| = 1/w$, cf (7) [16]. As w increases, creases are formed in the Möbius structure, which a quantum particle experiences as deepening potential wells which lower its energy. Figure 5 compares the energy level splitting for the exact Möbius strip and the approximation based on (17) for $L/2w = 30$, $L = 200$ Å found by solving (14). It is clear that for the lowest energies, the pattern of splitting is quite different. Recall though that the approximate shape completely fails to satisfy the constraint (18) at (still quite modest) larger widths. For low enough aspect ratio ($L/2w = 10\pi/13$), negative energy eigenstates appear, the usual signature for bound states. Note that this aspect ratio is much lower than that considered in [4, 14].

　　　Shown in figure 6 are the lowest energy wavefunctions for $Lk = 1/2$ at the four increasing widths of the structures shown in figures 1 and 4. For each plot, the horizontal axis
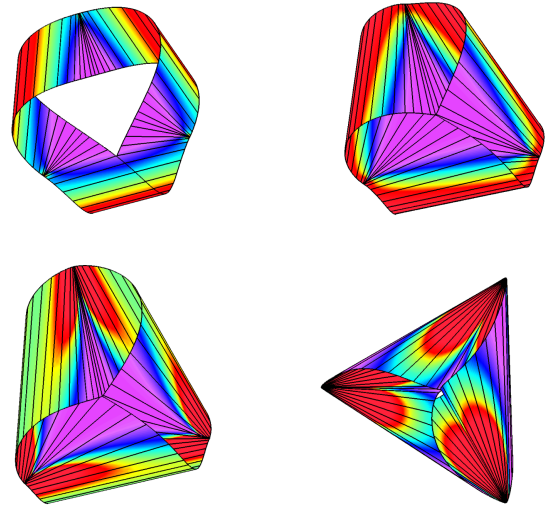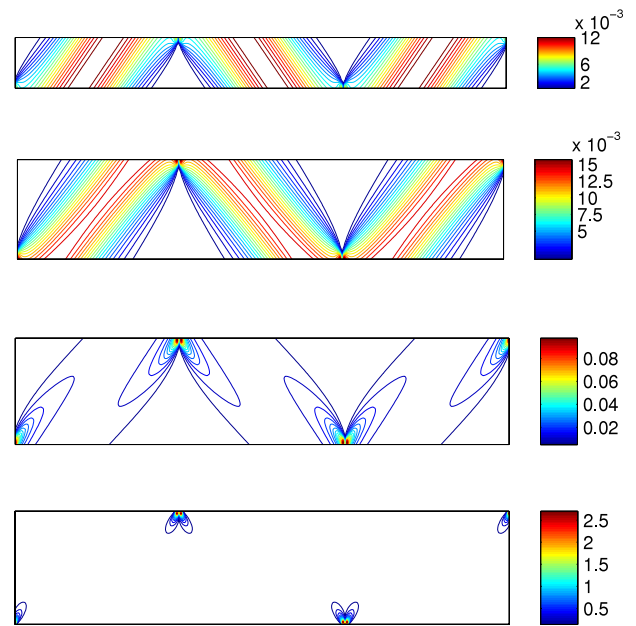

Figure 9. Scaled mean curvature squared of developed strip, $\frac{\hbar^2}{2m} M^2$, in eV for $Lk = 3/2$ and $L/2w = 9.36, 4.72, 4.49, 4.22$ (top to bottom). $u_1 \in [0, L]$, $u_2 \in [-w, w]$, $L = 200$ Å.

is $u_1 \in [0, L]$, $L = 200$ Å, the vertical axis $u_2 \in [-w, w]$. In each subfigure the lowest energy wavefunctions for each parity are shown using the order $(+, +)$, $(+, -)$, $(-, +)$, $(-, -)$ for the first, second, third and fourth rows respectively. The reflection symmetry of the wavefunctions is manifest. For the highest width, one can see evidence (first column of lower right subfigure) for the confinement of the lowest energy wavefunctions to the zigzag creases in the Möbius structure seen in figure 4 (bottom plot).

　　　Shown in figure 7 is the dimensionless energy $E' = (2mw^2/\hbar^2)E$ versus w, with negative energy states appearing
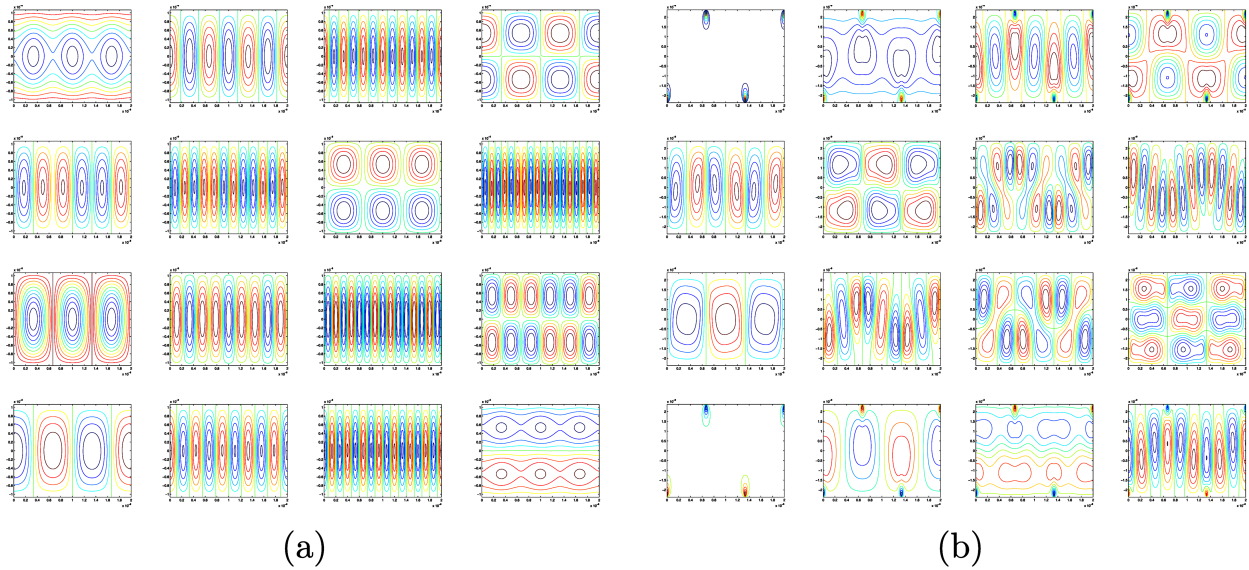
Figure 10. Lowest energy wavefunctions for $Lk = 3/2$. For each plot, the horizontal axis is $u_1 \in [0, L]$, $L = 200$ Å, the vertical axis $u_2 \in [-w, w]$. In each subfigure the lowest energy wavefunctions for each parity are shown using the order $(+, +)$, $(+, -)$, $(-, +)$, $(-, -)$ for the first, second, third and fourth rows respectively. (a) $L/2w = 9.36$; (b) $L/2w = 4.22$.

at the highest width. By comparison with the non-geometric (flat) strip (obtained with M^2 in (4) set to zero), we expect the energy to decrease with increasing width. There are therefore two competing effects. Multiplying E by w^2 makes E' increase with width initially, but for larger widths, a decreasing E' means that E decreases faster than $1/w^2$. The figure follows the lowest energy eigenstate for each parity with increasing width, with either one or two nodes in the u^1 direction, with a two-node eigenstate having the larger energy. Note that the states are not degenerate for the smallest width shown ($L/2w = 30$). Also, energy levels for states with more than one node in the u^2 direction would appear as further clusters of curves higher up the diagram.

3.4. Triple twist strip: $Lk = 3/2$

Shown in figure 8 are the exact $L/2w = 9.36, 4.72, 4.49, 4.22$ one-sided structures, with generators shown, of linking number $Lk = 3/2$. Note that there are now three alternatingly placed singularities on the edge of the strip where (18) is satisfied as an equality and the bending energy density M^2 goes to infinity. The top right structure just self-contacts in the middle. The larger-width structures in the bottom row were obtained by allowing for a non-zero reaction force (in the binormal direction) to prevent self-intersection. The corresponding contour plots of M^2 for the developed strips are shown in figure 9, for arbitrary length scale, with the three largest widths at self-contact. The symmetry arguments developed above for $Lk = 1/2$ carry over for $Lk = 3/2$ with the replacement $L \rightarrow L/3$. Thus κ, η, η' have the same reflection symmetry as in figure 2, with $L \rightarrow L/3$, and the same symmetry under the translation $s \rightarrow s + L/3$. These induce corresponding parity eigenstates (20) and (22) with L replaced with $L/3$. These are the so-called basically periodic solutions [32], which allow the domain to be reduced to $L/6$ for numerical integration

using the FD method. From the point of view of Bloch's theorem, $\chi(u^1 + L/3, u^2) = \exp(ikL/3)\chi(u^1, -u^2)$, with a Bravais lattice vector of magnitude $L/3$. To satisfy the periodic boundary condition kL must be an integer multiple of π. Here we only show solutions for $kL/3 = 0, \pi$.

As with Mathieu's equation, solutions of higher period exist [32], as long as the periodic boundary condition (16) is satisfied so that the wavefunction is single-valued. For example, to show solutions symmetric or anti-symmetric under translation $\chi(u^1, u^2) = \pm\chi(u^1 + L, -u^2)$ are induced by the underlying symmetry of κ, η, η' (i.e., exactly as for the single-twist Möbius strip), note that $s \rightarrow s + L$ induces $u^1 \rightarrow u^1 + L$ and that M^2 is invariant (η, η' and u^2 all change sign). Similarly, under the reflection, $s \rightarrow L - s, u^1 \rightarrow L - u^1$ and M^2 is invariant since η is even, but η' and u^2 change sign. From the point of view of Bloch's theorem, this corresponds to a Bravais lattice vector of magnitude L. For these higher periods fewer nodes are spread over the same length L, so more states of lower energies are observed, but not lower than the ground state obtained for the basically periodic solutions. Note that period $L/3$ implies period L but not vice versa.

Shown in figure 10 are the lowest energy wavefunctions for $Lk = 3/2$ at the four increasing widths of figures 8 and 9. For each plot, the horizontal axis is $u^1 \in [0, L]$, $L = 200$ Å, the vertical axis $u^2 \in [-w, w]$. In each subfigure the lowest energy wavefunctions for each parity are shown using the order $(+, +)$, $(+, -)$, $(-, +)$, $(-, -)$ for the first, second, third and fourth rows respectively. For the highest width, one can again see evidence for the confinement of the wavefunctions to potential wells corresponding to the bending energy density of the Möbius structure.

Shown in figure 11 is the dimensionless energy E' for $Lk = 3/2$. The figure again follows the lowest energy eigenstate for each parity with increasing width, with either one or two nodes in the u^1 direction, with a two-node eigenstate
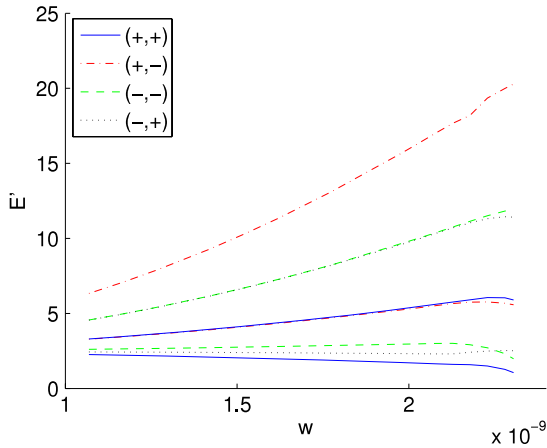
Figure 11. Dimensionless energy, E', for the lowest one- and two-node energy eigenstates for each parity ($Lk = 3/2$).

Figure 12. Dimensionless inverse participation ratio, A' ($Lk = 1/2$).

Figure 13. Dimensionless inverse participation ratio, A' ($Lk = 3/2$).

having the larger energy. Energy levels for states with more than one node in the u^2 direction would again appear as further clusters of curves higher up the diagram. The large-w energy behaviour does not now decrease faster than $1/w^2$. The $(-, -)$ and $(-, +)$ states also show a degeneracy at large w with the $(+, +)$ and $(-, -)$ approaching degeneracy at large w.

3.5. Curvature trapping of states

Much attention has been given to the degree of localization of states of particles constrained to move in structures with curvature [33, 34], with da Costa [19] giving the example of one bound state for the bookcover surface with a zero transmission coefficient in the case of an infinitely sharp bend. One measure used for distinguishing between localized and extended states is the inverse participation ratio [35, 36], $A = \int |\psi|^4 \, dV / (\int |\psi|^2 \, dV)^2$. The non-degenerate flat ground state $\chi = \cos(\pi u^2 / 2w)$ has dimensionless inverse participation ratio $A' \equiv A(2Lw) = 1.5$, whereas the flat higher excited states have $A' = 2.25$.

Shown in figure 12 is A' for $Lk = 1/2$, showing a general trend of increase in localization for increasing width. Comparison with the flat state values is perhaps not so meaningful for higher excited states as the flat states all have the same inverse participation ratio. The figure shows A', following the lowest energy eigenstate for each parity with increasing width.

Shown in figure 13 is the corresponding $A' \equiv A(2Lw/3)$ for $Lk = 3/2$. The flat values are the same as for $Lk = 1/2$. There is a marked increase of the inverse participation ratio with width, except for the $(-, +)$ state. There is a dip in the localization of the ground state before it also sharply increases with width.

The corresponding lowest energy wavefunctions are shown in figure 6 ($Lk = 1/2$) and figure 10 ($Lk = 3/2$) (first column of lower right subfigure) for the highest-width Möbius structures, showing confinement of the wavefunction to the high-curvature regions corresponding to the lowest plot in each of figures 4 and 9. The difference in topology is that $Lk = 3/2$ structures have no creases, prevented by self-contact, giving
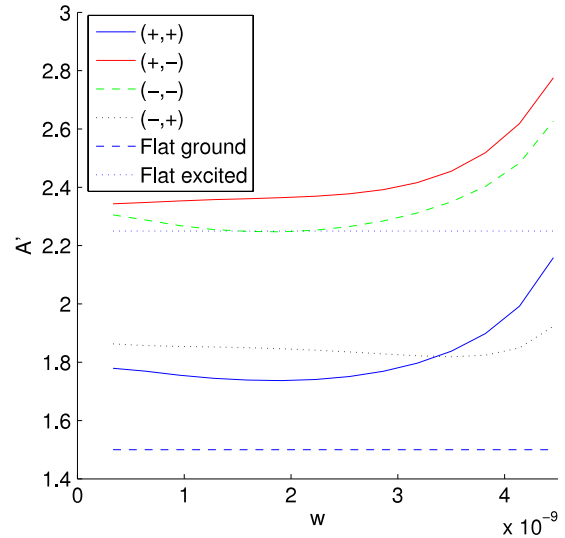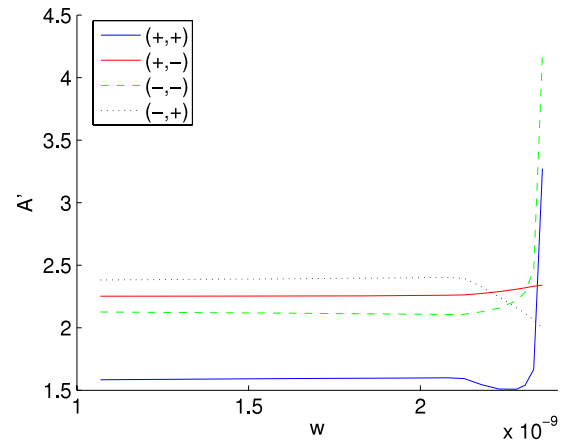
degenerate, disconnected, wavefunctions concentrated at the singularities in M^2 at the largest width. The $Lk = 1/2$ structures, by contrast, show localization to the creases formed at higher widths, allowing the wavefunction to be connected in a zigzag manner across the whole domain.

4. Conclusions

We have studied curvature effects of quantum particles confined to thin elastic sheets motivated by recent technological developments such as nanostructured origami [9] that allow for the fabrication and controlled folding of extremely thin membrane structures. The equilibrium shape of these sheets were found by minimizing the elastic energy, i.e., by solving the Euler–Lagrange equations for the bending energy functional. Contact forces may need to be accounted for in order to avoid self-intersection.

We have focused on rectangular one-sided surfaces (characterized by half-integer link), which, unlike two-sided

surfaces (characterized by integer link) are found to have singular points of diverging bending energy density on the edge of the surface, giving rise to deep surface potential wells for a particle on the surface. By solving the Schrödinger equation we have shown that electrons are increasingly localized (with corresponding negative energy states) to the high-curvature regions of the higher-width structures, especially for the Möbius strip, with $Lk = 1/2$, which develops an interconnected zigzag pattern of sharp creases. For the triple twist strip with $Lk = 3/2$, by contrast, the formation of sharp creases is resisted by contact forces.

As a measure for the electron localization we have obtained the inverse participation ratio as a function of the structure aspect ratio, both for $Lk = 1/2$ and $3/2$. Our geometric formulation could be used to study the transport properties of the Möbius strip, nanoribbon, and other folded-sheet components in nanoscale devices.

References

[1] Atanasov V and Dandoloff R 2008 *Phys. Lett.* A **372** 6141–4
[2] Atanasov V, Dandoloff R and Saxena A 2009 *Phys. Rev.* B **79** 033404
[3] Encinosa M and Jack M 2006 *Phys. Scr.* **73** 439–42
[4] Gravesen J and Willatzen M 2005 *Phys. Rev.* A **72** 032108
[5] Cantele G, Ninno D and Iadonisi G 2000 *J. Phys.: Condens. Matter* **12** 9019–36
[6] Dandoloff R and Truong T T 2004 *Phys. Lett.* A **325** 233–6
[7] Gridin D, Craster R V and Adamou A T I 2005 *Proc. R. Soc.* A **461** 1181–97
[8] Gridin D, Craster R V and Adamou A T I 2005 *Wave Motion* **42** 352–66
[9] Arora W J, Nichol A J, Smith H I and Barbastathis G 2006 *Appl. Phys. Lett.* **88** 053108
[10] Lagally M G 2007 *J. Phys.: Conf. Ser.* **61** 652–7
[11] Duan X, Niu C, Sahi V, Chen J, Parce J W, Empedocles S and Goldman J L 2003 *Nature* **425** 274–8
[12] Jensen H, Kroger J and Berndt R 2005 *Phys. Rev.* B **71** 155417
[13] Tanda S, Tsuneta T, Okajima Y, Inagaki K, Yamaya K and Hatekenata N 2002 *Nature* **417** 397–8
[14] Caetano E W S, Freire V N, dos Santos S G, Galvão D S and Sato F 2008 *J. Chem. Phys.* **128** 164719
[15] Cerda E and Mahadevan L 2005 *Proc. R. Soc.* A **461** 671–700
[16] Starostin E L and van der Heijden G H M 2007 *Nat. Mater.* **6** 563–7
[17] Gravesen J, Willatzen M and Voon L Y 2005 *J. Math. Phys.* **46** 012107
[18] Safran S A 2003 *Statistical Thermodynamics of Surfaces, Interfaces, and Membranes* (Boulder, CO: Westview Press)
[19] da Costa R C T 1981 *Phys. Rev.* A **23** 1982–7
[20] Schuster P C and Jaffe R L 2003 *Ann. Phys., NY* **307** 132–43
[21] Graustein W C 1966 *Differential Geometry* (New York: Dover)
[22] Love A E H 1927 *A Treatise on the Mathematical Theory of Elasticity* (Cambridge: Cambridge University Press)
[23] Randrup T and Røgen P 1996 *Arch. Math.* **66** 511–21
[24] Wunderlich W 1962 *Monatsh. Math.* **66** 276–89
[25] Starostin E L and van der Heijden G H M 2009 *Phys. Rev.* E **79** 066602
[26] Bawin M and Burnel A 1985 *J. Phys. A: Math. Gen.* **18** 2123–6
[27] Merzbacher E 1962 *Am. J. Phys.* A **30** 237–47
[28] Ashcroft N W and Mermin N D 1976 *Solid State Physics* (Fort Worth: Saunders)
[29] Fuller F B 1978 *Proc. Natl Acad. Sci. USA* **75** 3557–61
[30] Maiti S K 2007 *Solid State Commun.* **142** 398–403
[31] McCulloch I P 2007 *J. Stat. Mech* P10014
[32] Arscott F M 1964 *Periodic Differential Equations* (Oxford: Pergamon)
[33] Hurt N E 2000 *Mathematical Physics of Quantum Wires and Devices: From Spectral Resonances to Anderson Localization* (Dordrecht: Kluwer Academic)
[34] Goldstone J and Jaffe R L 1992 *Phys. Rev.* B **45** 14100–7
[35] Thouless D J 1974 *Phys. Rep.* **13** 93–142
[36] Taira H and Shima H 2007 *J. Phys.: Conf. Ser.* **61** 1142–6